Insights into key parameters of MnO_2 catalyst towards high catalytic combustion performance

Luming Li [a, b, c], Wei Chu [a*], Yan Liu [b*]

[a] Department of Chemical Engineering, Sichuan University, Chengdu 610065, China

[b] Institute of Chemical and Engineering Sciences, A*STAR, 627833, Singapore

[c] Institute for Advanced Study, Chengdu University, Chengdu 610065, China

* **Corresponding authors:** E-mail: liu_yan@ices.a-star.edu.sg (Y. Liu),

chuwei1965@scu.edu.cn (W. Chu).

Abstract: Controllable crystal phases (α-, β-, γ- and δ-) of MnO_2 materials were developed via tuning hydrothermal conditions and investigated in toluene catalytic combustion. Extensive characterization techniques such as XRD, BET, SEM, TEM, H_2-TPR and XPS were employed for analyzing the structure-performance relationship between physicochemical properties, such as specific surface area, vacancy/lattice oxygen and their mobility, reduction property and catalytic activity. Results indicated that the degradation activity of MnO_2 catalyst greatly hinges on materials intrinsic properties, namely the vacancy oxygen generation, lattice oxygen content and their reduction behaviors. α-MnO_2 exhibited the best catalytic activity (0.24 μmol/min @ 240 °C) among the obtained MnO_2 materials, however its cycle stability was inferior to that of δ-MnO_2 catalyst owing to the different moderating effect of potassium ions remained within the tunnels or mezzanines structure. In addition, δ-MnO_2 showed an easiest reduction property

among all the manganese oxides investigated. The findings will shed lights on designing of Mn-based catalysts with a higher VOCs combustion capacity.

Keywords: MnO_2; Crystalline phase; Potassium; VOCs; Structure-performance relationship.

1. Introduction

Volatile organic compounds (VOCs), one of the major pollutants, have seriously affected on the ecological environment and the sustainable development of human society. Therefore, it is urgent to adopt some technical strategies to effectively prevent and control VOCs emission. Up to now, techniques such as high-temperature incineration, absorption, membrane separation, biodegradation, photocatalysis, plasma, catalytic oxidation have been developed. Specifically, catalytic combustion has been regarded as one of the most effective techniques towards VOCs abatement because it can completely convert VOCs molecular into CO_2 and H_2O without formation of secondary products such as NOx under a relatively low reaction temperature (≤400 ºC) [1-4]. To design and synthesize catalysts with high catalytic activity and low cost is the key for catalytic degradation of VOCs.

The reports on VOCs degradation catalysts can be mainly classified as noble and non-noble metal catalysts. Although noble metal catalysts own an excellent catalytic activity, some disadvantages must be taken into consideration such as scarce natural reserves and high cost, which hinders its industrial applications to some extent. Hence, the development of substitutes for noble metals has become an important scientific direction [5, 6]. It was reported that transition oxide such as MnO_x catalyst exhibited great potential as an alternative to noble metal

catalysts due to its high oxygen storage capacity, polyvalence and redox properties [7-9]. However, it is found that the MnO_2 possesses various structures attributing to different construction modes of [MnO_6] unit, which may lead to different physicochemical properties. It is necessary to study the key factors of MnO_2 catalysts towards controlling catalytic capacity for VOCs degradation.

Wang et al compared toluene combustion activity of rod-shaped, wire and tube α-MnO_2 and flower-like Mn_2O_3 catalysts, and found that the catalytic activity order follows: rod-shaped α-MnO_2 > tube α-MnO_2 > flower-like Mn_2O_3 > wire α-MnO_2. It was also observed that the order of catalytic activity was consistent with the decreasing of surface adsorbed oxygen, indicating that surface adsorbed oxygen concentration played a vital role in catalytic oxidation of toluene [10]. Zhang et al studied the structure-activity relationship between the crystalline phases of MnO_2 and their corresponding catalytic activities for HCHO combustion. The results showed that δ-MnO_2 catalyst with the highest lattice oxygen concentration gave the best catalyst activity among different phases (α-, β-, γ- and δ-) MnO_2 catalysts [11]. However, Zhu et al found that the catalytic activity order of MnO_2 catalysts for CO oxidation is α- ≈ δ- > γ- > β-MnO_2 [12]. Lu et al reported that the activity sequence of MnO_2 catalysts towards propane combustion followed α- ≈ γ- > β- > δ-MnO_2. Their catalytic activity mainly depends on the crystal phase because different crystal phase would lead to different adsorption energy of propane [13]. In view of the reports, the relationship between the structural factors and catalytic performance for MnO_2 catalyst is ambiguous. A detailed study on the structure-activity relationship of MnO_2 catalysts is needed. In this contribution, series of MnO_2 catalysts with various crystalline phases (α-, β-, γ- and δ-) have been controllably synthesized by tuning

different hydrothermal conditions and their catalytic performance were evaluated on toluene combustion experiment. Toluene, as a typical VOCs molecule, which is widely used as industrial solvent and is difficult to be oxidized at low temperature due to its stable molecular structure, was chosen as a probe molecule for studying the structure-catalytic performance relationship of MnO_2 materials. Results indicated that α-MnO_2 exhibited the best catalytic activity (0.24 μmol/min @ 240 ºC) among the obtained MnO_2 materials, however its cycle stability was inferior to that of δ-MnO_2 catalyst owing to the different moderating effect of potassium ions remained within the tunnels (α-MnO_2) or mezzanines (δ-MnO_2) structure.

2. Experimental

2.1 Catalysts preparation

All MnO_2 catalysts were prepared via modified hydrothermal process based on literatures [13, 14]. α-MnO_2-10h: 1.2 g of $KMnO_4$ and 0.5 g of $MnSO_4 \cdot H_2O$ were added into 60 mL of de-ionized water, and stirred for 30 min to form a homogeneous solution. Then, this mixture solution was transferred into a Teflon-lined stainless steel autoclave and maintained at 160 °C for 10 h. And the generated solid product was filtered, washed to remove the impurities such as SO_4^{2-} and K^+. Finally, the obtained sample was dried at 100 °C in air for 20 h. Similarly, β-MnO_2-10h and δ-MnO_2-10h catalysts can be prepared via the same hydrothermal procedures, except for the different added content of $KMnO_4$ and $MnSO_4 \cdot H_2O$. $KMnO_4$ and $MnSO_4 \cdot H_2O$ were 0.5 g and 2.5 g for preparation of β-MnO_2-10h catalyst, while for generating δ-MnO_2-10h sample, they are 2.8 g and 0.5 g, respectively. For preparation of γ-MnO_2-20h catalyst, 2.7 g of

$MnSO_4 \cdot H_2O$ and 3.7 g of $(NH_4)_2S_2O_8$ were mixed, and hydrothermally treated at 90 °C for 20 h. When it comes to the δ-MnO_2-48h catalyst, 3.6 g $Mn(NO_3)_2$ solution and 3.2 g $KMnO_4$ were added into the 40 mL of water, followed the similar above mentioned treatment procedures, except for the hydrothermal temperature (50 ºC) and time (48 h).

2.2 Catalyst characterization

The crystal phase of the prepared catalysts were investigated by X-ray diffraction (XRD) using a DX-2700 with Cu Kα X-ray source (λ=1.542 Å) in a step scan mode with a scanning rate of 0.03°/s in the range from 5° to 80°. Micromeritics ASAP 2420 instrument was employed to measure the specific surface areas and pore size distribution of the catalysts. Prior to analysis, each sample was degassed at 200 ºC for 12 h to remove physically adsorbed impurities. Scanning electron microscopy (SEM) was performed on a JEOL SM71010 microscope. The sample was deposited onto a double face graphite tape in order to avoid the problem of charging effect during the analysis. FEI Tecnai G2 F20 microscope equipped with a HAADF detector were used to investigate the microstructural of the fresh MnO_2 samples, namely transmission electron microscopy (TEM) analysis. Chemical state of surface elements was investigated by X-ray photoelectron spectroscopy (XPS, XSAM800) using Al Kα as an exciting X-ray source. The spectra were calibrated with respect to the C 1s peak of adventitious carbon at 284.6 eV. The hydrogen temperature programmed reduction (H_2-TPR) experiment was carried out on a chemisorption Analyzer (AutoChem 2920) with a thermal conductivity detector (TCD). After sweeping by reduction gas of 5% H_2/N_2 with a total gas flow rate of 30 mL/min. the temperature of the reactor was raised linearly from 100 ºC to 750 ºC at a heating rate of 10 ºC/min. The H_2

consumption was recorded by thermal conductivity detector (TCD) after removal of produced H_2O.

2.3 Catalytic activity testing

Catalytic activities for the toluene degradation experiment was performed on a fixed-bed quartz reactor (i.d. = 8 mm) in an electric furnace. 100 mg of 40-60 mesh catalyst was loaded in the center of the reactor. Prior to catalytic experiment, the catalyst was pretreated in air with a flow-rate of 60 mL/min at 150 ºC for 1 h. The reaction feed gas consisted of 1000 ppm of toluene in air balance gas. The total flow was 50 mL/min, at a gas hour space velocity (GHSV) of 30 000 ml/(g·h). The emitted gases after toluene combustion were analyzed online using a SP-6890 gas chromatograph equipped with a flame ionization detector (FID) and a thermal conductivity detector (TCD). The conversion of toluene was evaluated based on the mole amount of inlet and outlet toluene. Before collecting the analysis of reactant concentration at each sampling point, the reaction temperature was maintained for at least 30 min for reaching a steady state.

$$x_{Tol}(\%) = \frac{c_{in} - c_{out}}{c_{in}} \cdot 100\% \quad \text{(Eq. 1)}$$

where, x_{Tol} indicates toluene conversion, c_{in} (ppm) and c_{out} (ppm) indicate the reactor's inlet and outlet toluene concentration, respectively.

The reaction rate over catalysts is calculated using the following Eq. 2:

$$R(\mu mol\ min^{-1}) = v_{Tol} \cdot x_{Tol} \quad \text{(Eq. 2)}$$

where R ($\mu mol\ min^{-1}$) is the reaction rate of toluene combustion at a certain temperature, v_{Tol} ($\mu mol\ min^{-1}$) is the toluene gas flow; x_{Tol} is the conversion of toluene.

The specific reaction rate over catalysts is calculated using the following Eq. 3:

$$R_s\left(\mu mol\ {m_{cat}}^{-2} min^{-1}\right) = \frac{\nu_{Tol} \cdot x_{Tol}}{W_{cat} \cdot S_{cat}} \quad \text{(Eq. 3)}$$

where R_s ($\mu mol\ {m_{cat}}^{-2} min^{-1}$) is the reaction rate of toluene combustion; ν_{Tol} ($\mu mol\ min^{-1}$) is the toluene gas flow; x_{Tol} is the conversion of toluene at a certain temperature; W_{cat} is the weight of catalyst employed (0.1g); S_{cat} is the BET surface area of catalyst.

3. Results and discussion

3.1 XRD analysis

The XRD patterns of the freshly synthesized MnO_2 catalysts with different crystal phases under different hydrothermal conditions were presented Figure 1a. It was observed that XRD patterns of target MnO_2 samples (α-, β-, γ- or δ-MnO_2) correspond well with the standard PDF number, which are 44-0141, 24-0735, 14-0644 and 80-1098, respectively. No other phases were detected, indicating pure crystalline phases were obtained. It suggests that the hydrothermal conditions we adopted are suitable for controllable synthesis of various MnO_2 crystal phase with high quality. It was well accepted that the crystallinity of the product can be expressed based on the intensity and width of XRD peak [13]. We found that the peaks intensity of γ- and δ-MnO_2 catalyst is apparent lower than that of α- and β-MnO_2 products, confirming there exists different level of crystallinity for MnO_2 with different crystal phases. According to the average crystal sizes of fresh MnO_2 samples calculated by Scherrer's equation, as listed in Table 1, we observed that the grain size order follows: δ-MnO_2-48h (6.2 nm) < δ-MnO_2-10h (10.5 nm) < α-MnO_2-10h (17.1 nm) < γ-MnO_2-20h (18.8 nm) < β-MnO_2-10h (27.2 nm). It revealed that the

grain size of target MnO_2 catalyst was determined by both the crystalline structure and hydrothermal condition. For example, the grain size of β-MnO_2-10h sample (27.2 nm) is the largest among the obtained products, though the hydrothermal temperature is only 90 °C. However, the lower hydrothermal temperatures induced the formation of smaller grain sizes with poor crystallinity for MnO_2 catalyst with the same crystalline structure to some extent.

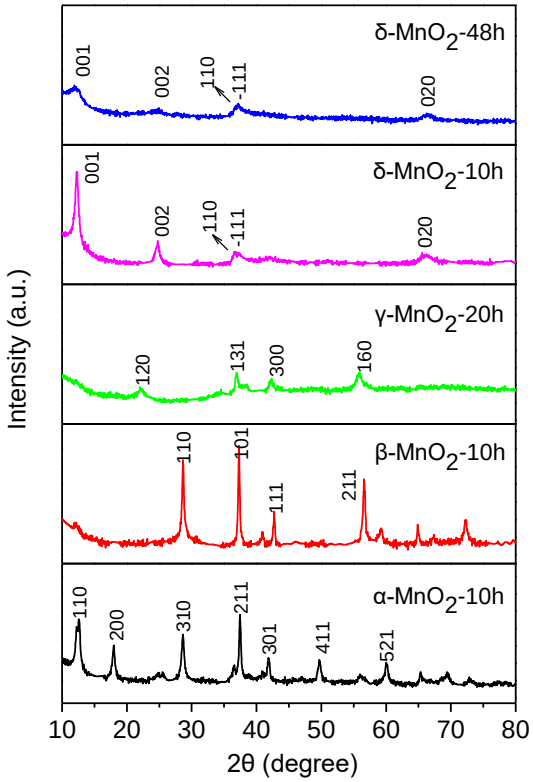

Figure 1 XRD patterns of MnO_2 catalysts under different hydrothermal conditions

Table 1. The specific areas, particle size and H_2 consumption of MnO_2 prepared under different hydrothermal conditions.

Catalysts	S_{BET} (m^2/g)	Grain size [a] (nm)	H_2 consumption [b] (mmol/g)
α-MnO_2-10h	51.8	17.1	6.32
β-MnO_2-10h	15.5	27.2	7.53

γ-MnO_2-20h	76.1	18.8	6.65
δ-MnO_2-10h	15.5	10.5	5.13
δ-MnO_2-48h	57.0	6.2	5.03

a) Calculated by Scherrer's equation.

b) Calculated from H_2-TPR analysis.

3.2 MnO_2 Microstructure and morphologies

Generally, the specific surface area and pore structure of the catalyst have great influence on its catalytic activity. In order to study structure-performance relationship of MnO_2 with different crystalline structure, N_2 adsorption desorption experiment was carried out, as depicted in Figure 2a and Table 1. We can observe that the α- and δ-MnO_2 catalysts exhibits a typical type IV isotherm with a broad value of relative isotherm pressures between 0.4 - 1.0, implying that both of them have a typical mesoporous structure according to the classification of IUPAC [15, 16]. However, the value range of relative isotherm pressures becomes narrower for γ-MnO_2-20h sample (0.6 - 1.0) and for β-MnO_2-10h product (0.9 - 1.0). The pore-size distribution curves calculated from the Barrett–Joyner–Halenda (BJH) method were showed in Figure 2b. It can be seen that α-MnO_2-10h and δ-MnO_2-48h catalysts have a much narrower pore size distribution at about 4.0 nm, but pore size distribution is pretty wide at around 12.0 nm for γ-MnO_2-20h sample, in good agreement with the results of N_2 adsorption desorption. In value of specific surface area, the BET surface areas were calculated to be 76.1, 57.0, 51.8, 15.5 and 15.5 m^2/g, for γ-MnO_2-20h, δ-MnO_2-48h, α-MnO_2-10h, δ-MnO_2-10h and β-MnO_2-10h sample, respectively.

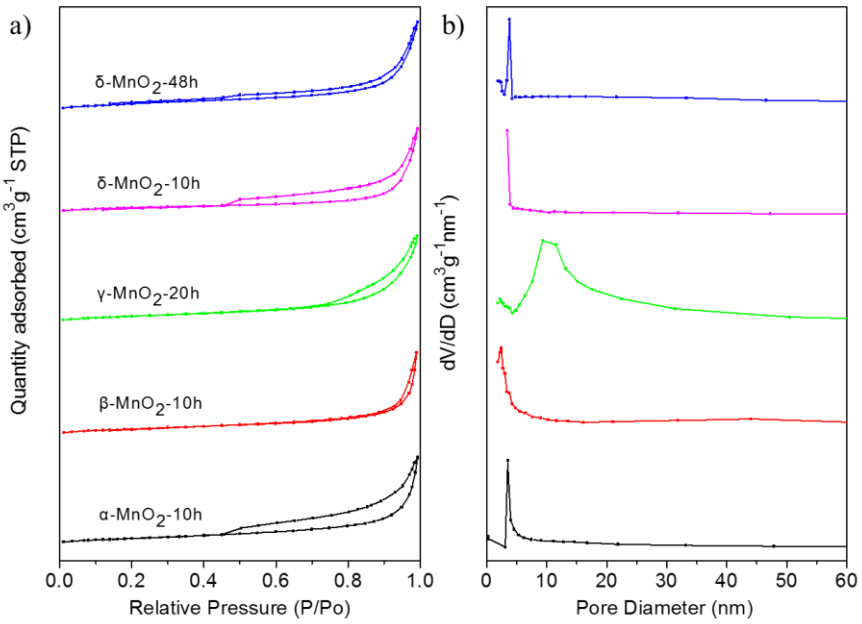

Figure 2 Nitrogen physisorption isotherms (A) and pore size distributions (B) of MnO_2 catalysts under different hydrothermal conditions.

The morphology of MnO_2 catalyst was examined by SEM technique, as depicted in Figure 3. It revealed that both α-MnO_2-10h (Figure 3a) and β-MnO_2-10h (Figure 3b) samples are composed of nanorods, with the diameter varying from 20 to 100 nm, at micron-sized length. γ-MnO_2-20h catalyst (Figure 3c) consists of irregular rod-like shape. Impressively, δ-MnO_2-10h（Figure 3d）and δ-MnO_2-48h（Figure 3e）demonstrates flower-like morphology composed of ultrathin nanoplates, with ca. 10 nm in thickness. It is noted that the diameter of flower-like of δ-MnO_2-48h is slight smaller than that of δ-MnO_2-10h sample, which is mainly resulted from the lower hydrothermal temperature.

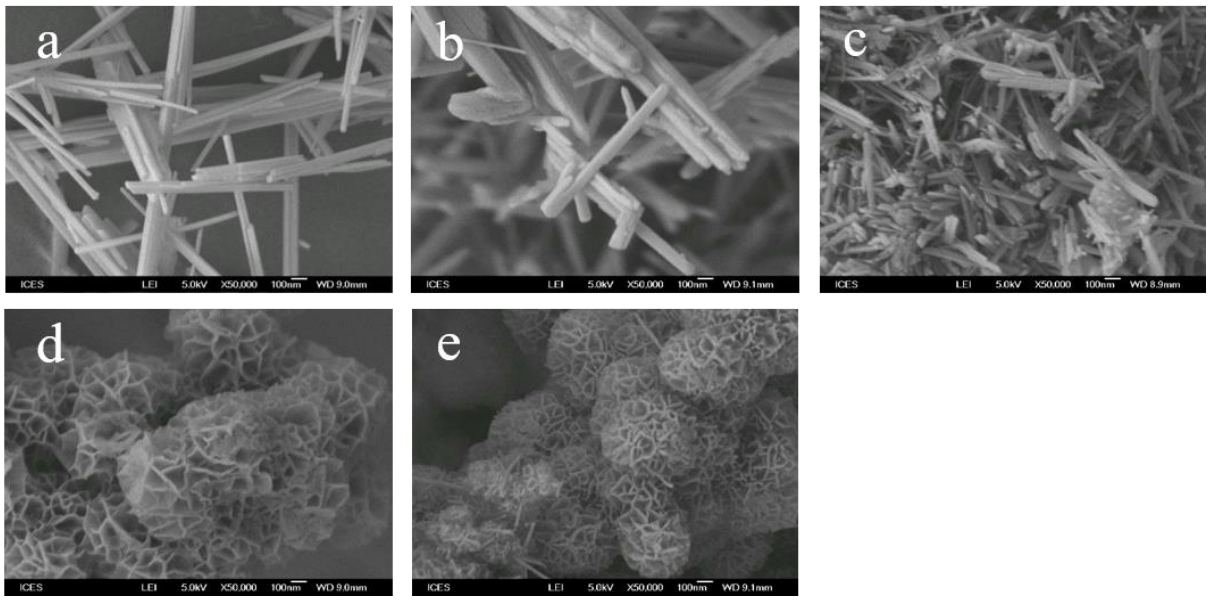

Figure 3 The SEM images of the different phase of MnO_2; (a) α-MnO_2-10h, (b) β-MnO_2-10h, (c) γ-MnO_2-20h, (d) δ-MnO_2-10h; (e) δ-MnO_2-48h.

TEM measurement is a power technique to directly observe the microstructure and confirm the crystal indices through the calculated plane spacing (HRTEM). Figure 4 displayed the TEM and HRTEM images of the α-MnO_2-10h，δ-MnO_2-10h and δ-MnO_2-48h catalysts. Those further prove that α-MnO_2 catalyst are composed of nano-rods (Figure 4a), while δ-MnO_2 sample with flower-like morphology (Figures 4c and 4e) was assembled by ultrathin nano-sheets. The calculated crystal plane spacing of 6.9 Å and 2.4 Å should be considered as the corresponding crystal plane of (110) and (210) for α-MnO_2 catalyst (Figure 4b). About 6.7 nm of crystal plane spacing should be attributed to the crystal plane of (100) for δ-MnO_2 sample. The results well correspond with the XRD results shown in Figure 1.

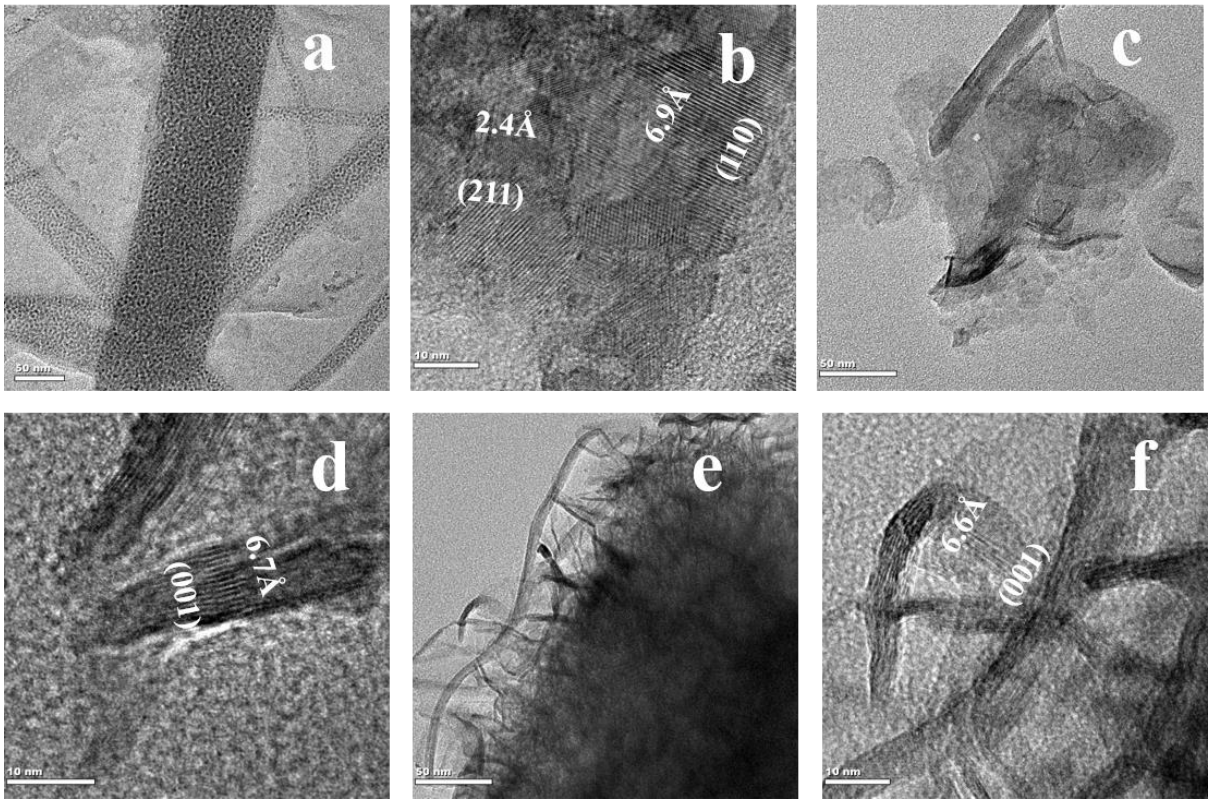

Figure 4 TEM and HRTEM of obtained samples: α-MnO_2-10h (a and b), δ-MnO_2-10h (c and d), δ-MnO_2-48h (e and f).

3.3 Reduction behavior

H_2-TPR testing was employed to study the reduction capacity of the fresh MnO_2 catalysts as pictured in Figure 5. For β-MnO_2-10h sample, there existed two peaks of H_2 consumption, which were respectively low temperature reduction peak at 330 ^oC and high temperature reduction peak at 423 ^oC. The low temperature reduction was assigned to the MnO_2 reduction to Mn_3O_4, while high temperature reduction should be linked to Mn_3O_4 reduced to MnO [11]. The H_2-TPR typical peaks of the γ-MnO_2-20h catalyst were similar to those of β-MnO_2-10h sample, but shifting to the lower temperatures, at 300 and 394 ^oC, respectively. Results verified

that the γ-MnO_2-20h performs a better reduction property than that of β-MnO_2-10h catalyst. However, the reduction behavior of α-MnO_2-10h and δ-MnO_2-10h catalysts is obviously different from the β-MnO_2-10h and γ-MnO_2-20h samples. As displayed in Figure 5, an overlapping reduction peak emerged, which was probably assigned to the coexistence of Mn_2O_3 and Mn_3O_4 intermediates [17]. Particularly for α-MnO_2-10h catalyst, even though its two reduction peaks located at 306 °C and 325°C were higher than those for δ-MnO_2-10h at 255 and 305 °C, α-MnO_2-10h is easier to be completely reduced than that of δ-MnO_2-10h catalyst because of the verified lower termination temperature of reduction. In addition, the reduction temperature position was similar for the δ-MnO_2-10h and δ-MnO_2-48h catalysts. However, the δ-MnO_2-48h sample demonstrated the lower termination temperature of reduction, inferring that the lower hydrothermal temperature could leads to the better reduction capacity for MnO_2 catalyst with the same crystalline structure. In view of reduction temperature, it can be speculated that the order of reduction easiness was δ-MnO_2-48h > α-MnO_2-10h > δ-MnO_2-10h > γ-MnO_2-20h > β-MnO_2-10h.

Furthermore, the hydrogen consumption was calibrated with CuO as the standard reference. It was observed that the order of hydrogen consumption followed as β-MnO_2-10h (7.53 mmol/g) > γ-MnO_2-20h (6.65 mmol/g) > α-MnO_2-10h (6.32 mmol/g) > δ-MnO_2-10h (5.13 mmol/g) ≈ δ-MnO_2-48h (5.03 mmol/g), as summarized in Table 1. The hydrogen consumption of all samples was lower than the theoretical value (11.5 mmol/g), which may be due to the formation of Mn^{3+}. The value of hydrogen consumption for α-MnO_2 and δ-MnO_2 was lower than that of β-MnO_2 sample, probably originating from the co-existence of K^+ and the higher concentration of water during the preparation processes [18, 19].

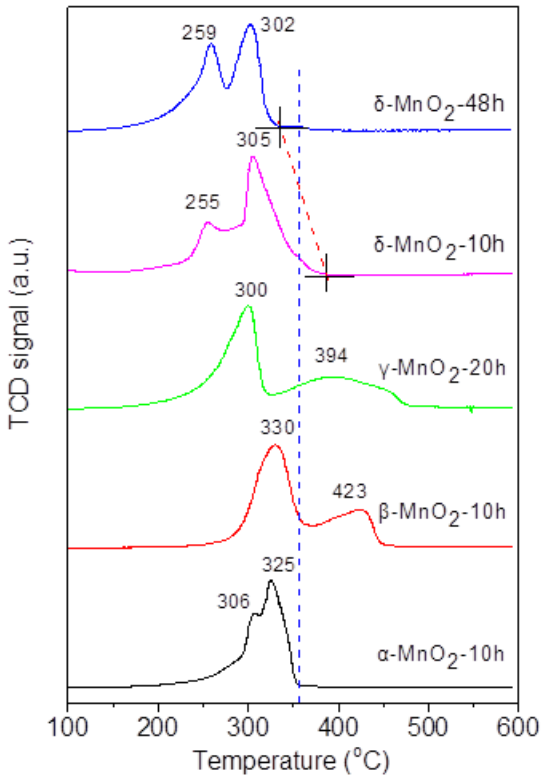

Figure 5 H_2-TPR profiles of MnO_2 catalysts

3.4 XPS analysis

The surface element composition and its content of the catalyst were collected by XPS analysis, as shown in Figure 6 full spectrum. It was observed that the element composition of α-MnO_2-10h，δ-MnO_2-10h and δ-MnO_2-48h catalysts were composed of C, K, O and Mn, while γ-MnO_2-20h and β-MnO_2-10h consisted of C, O and Mn. It was reported that K^+ in the tunnels (α-MnO_2) or mezzanines (δ-MnO_2) can balance the charge or stabilize the crystalline structure for both α- and δ-MnO_2 [20-22]. In addition, for bonding energy of K2s at 291.9 and 294.8 eV, we noticed that the K^+ content of α-MnO_2-10h and δ-MnO_2-10 sample was higher than that of δ-MnO_2-48h based the peak intensity of K2s (Figure 6), agreed by the comparison

of K2s XPS spectra of δ-MnO_2-10h and δ-MnO_2-48h in Figure 7.

Correlating with the above H_2-TPR reduction behavior analysis in Figure 5, it was further verified that the co-existence of K^+ with a relative high concentration resulting in the less hydrogen consumption content of α-MnO_2-10h，δ-MnO_2-10h and δ-MnO_2-48h catalysts than the theoretical value. However, the lower content of K^+ for δ-MnO_2-48h catalyst won't lead to the slight decreasing of hydrogen consumption compared to that for δ-MnO_2-10h, which was mainly linked to the formation of Mn^{3+} at a higher content in δ-MnO_2-48h catalyst, as shown in Table 2 [23].

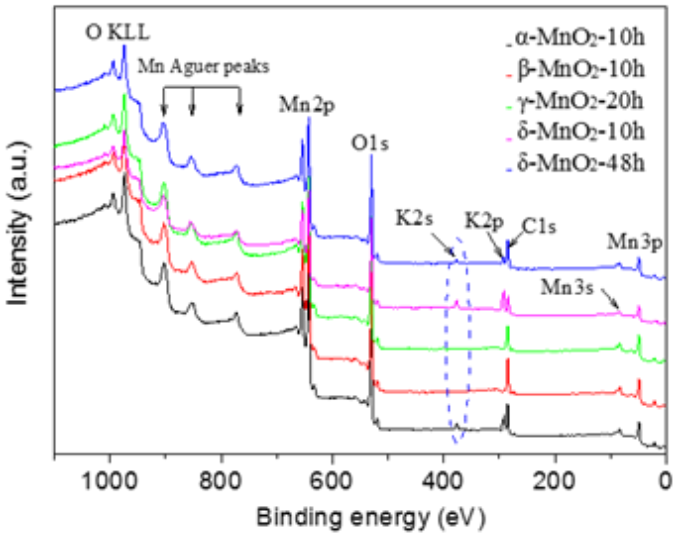

Figure 6 XPS full spectra of MnO_2 catalysts.

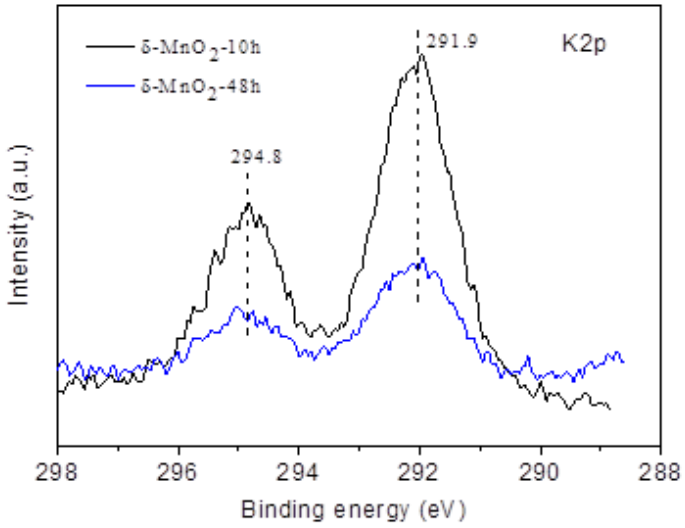

Figure 7 K2p XPS spectra of δ-MnO_2-10h and δ-MnO_2-48h samples

In addition, the content of Mn^{4+} for all the MnO_2 catalysts are summarized based on the Lorentzian-Gaussian peak fitting of $Mn2p_{3/2}$, as presented in Figure 8 and Table 2. It was found that the $Mn2p_{3/2}$ spectra for all the fresh MnO_2 sample can be deconvoluted into two peaks located at around 641.9 and 642.7 eV, well corresponding to the Mn^{3+} and Mn^{4+} species [11, 24]. By calculating the relative peak areas of Mn species (Table 2), it was concluded that the concentration of Mn^{4+} is higher than 65% in all the MnO_2 catalysts, suggesting Mn^{4+} is the dominant species for the synthesized MnO_2 catalysts via hydrothermal process, as reported by Zhu's group [12]. The decreasing order of Mn^{4+} concentration follows: δ-MnO_2-10h (86.7%) > δ-MnO_2-48h (81.5%) > γ-MnO_2-20h (80.3%) > β-MnO_2-10h (77.8%) > α-MnO_2-10h (66.9%). Results implied that the concentration of Mn^{4+} can be moderating via tuning the hydrothermal conditions. The low hydrothermal temperature probably induces the formation of surface defects, leading to a decrease of Mn valence state.

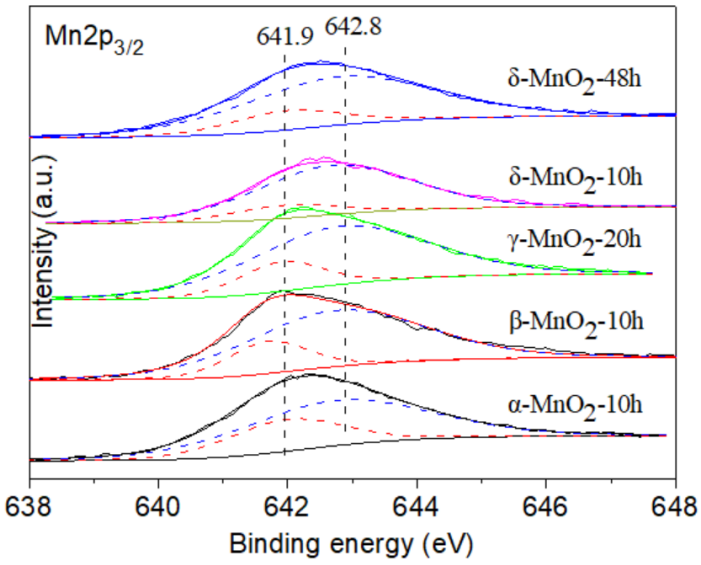

Figure 8 Mn2p XPS spectra of the prepared MnO_2 catalysts.

Table 2 The binding energy position of Mn2p and O1s and their concentrations.

Catalysts	Bind energy (eV)		Mn^{4+}	Bind energy (eV)		O_{latt} content
	Mn^{4+}	Mn^{3+}	content (%)	O_{latt}	O_{ads}	(%)
α-MnO_2-10h	642.7	641.9	69.9	529.6	531.4	73.2
β-MnO_2-10h	642.7	641.9	77.8	529.4	531.2	65.9
γ-MnO_2-20h	642.8	641.9	80.3	529.7	531.7	67.7
δ-MnO_2-10h	642.8	641.9	85.0	529.8	531.8	85.4
δ-MnO_2-48h	642.8	641.9	81.5	529.8	531.8	73.9

It was well-known that the lattice oxygen is regards as the catalytic active and adsorptive sites for majority of MnO_2 based catalysts [25-27]. Figure 9 showed the O1s spectra of the obtained MnO_2 catalyst. There exhibited two oxygen species on the surface of all catalysts. The binding energy at 529.6 ± 0.2 eV is the characteristic peak of lattice oxygen, while the characteristic peak at 531.5 ± 0.3 eV presents the adsorbed oxygen. The lattice oxygen

concentration is much higher than that of adsorbed oxygen, which follows the descending order as δ-MnO_2-10h (85.4%) > δ-MnO_2-48h (73.9%) > α-MnO_2-10h (73.2%) > γ-MnO_2-20h (67.7%) > β-MnO_2-10h (65.9%). The decreasing trend of lattice oxygen concentration was basically related to the decreasing trend of Mn^{4+} concentration except for the α-MnO_2-10h, indicating that the lattice oxygen concentration of the catalyst was positively correlated with the content of Mn^{4+}. High concentration of Mn^{4+} leads to the high concentration of lattice oxygen.

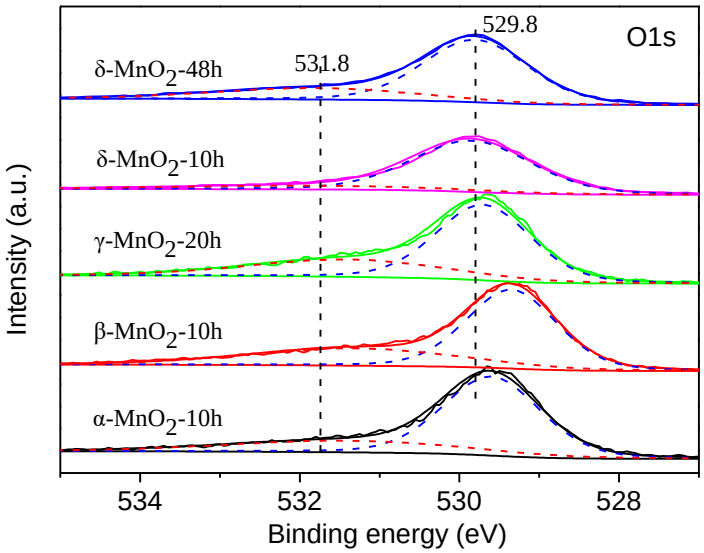

Figure 9 O1s XPS spectra of the prepared MnO_2 catalysts.

3.5 Toluene catalytic activity

Before the catalytic activity testing, the blank experiment should be carried out and the activity result of diluent (SiO_2) has been confirmed a negligible catalytic degradation activity towards toluene total oxidation. Figure 10 presented the toluene combustion activity of prepared MnO_2 catalysts. It was found that the catalytic activity increases as the function of reaction temperature. Up to 90% toluene conversion was achieved for all MnO_2 catalysts below

310 °C, indicating MnO_2 based catalysts performs a good abatement capacity for toluene. However, the MnO_2 catalyst with different crystal phase or physiochemical property exhibited the various toluene degradation activity. α-MnO_2-10h has the lowest T_{50} (the conversion of 1000 ppm toluene is 50%) and T_{90} (the conversion of 1000 ppm toluene is 90%) temperatures at 241 and 248 °C, followed by δ-MnO_2-48h catalysts at 251 and 258 °C, as summarized in Table 3. The order of catalytic oxidation capacity is depicted as α-MnO_2-10h > δ-MnO_2-48h > γ-MnO_2-20h > δ-MnO_2-10h > β-MnO_2-10h, implying that catalytic activity of MnO_2 has a certain correlation with its crystal phase. However, it is not absolute. The preparation conditions must be taken into consideration before the structure-activity relationship will be discussed. For example, as indicated in Table 3, δ-MnO_2-48h catalyst displayed a better catalytic capacity towards toluene oxidative degradation than that of δ-MnO_2-10h and γ-MnO_2-20h samples by regulating the hydrothermal conditions. Combined with the above analysis, the improved catalytic performance of δ-MnO_2-48h sample should be attributed to the higher surface occupation of oxygen vacancy formed from their poor crystallinity due to low hydrothermal synthesis temperature.

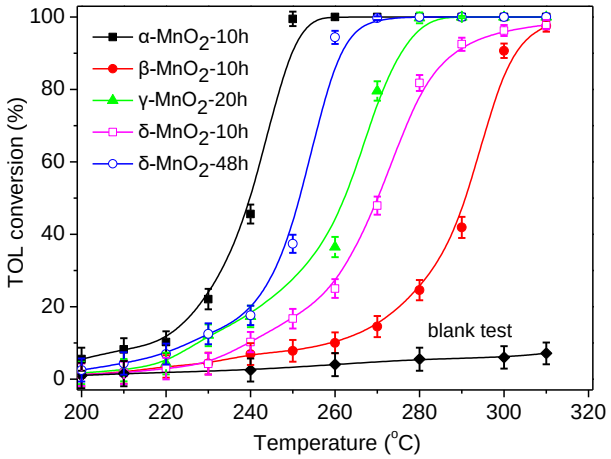

Figure 10 Effect of hydrothermal condition towards catalytic activity of MnO_2 catalysts for toluene combustion.

Table 3 T_{50}, T_{90}, reaction rate and specific rate of toluene oxidation over the catalysts.

Catalysts	Catalytic activity (°C)		Rate at 240°C	Specific rate at 240°C	Rate at 260°C	Specific rate at 260°C
	T_{50}	T_{90}	(μmol min^{-1})[a]	($\mu mol\ m_{cat}{}^{-2} min^{-1}$)[b]	(μmol min^{-1})[a]	($\mu mol\ m_{cat}{}^{-2} min^{-1}$)[b]
α-MnO_2-10h	241	248	0.24	0.047	0.52	0.10
β-MnO_2-10h	291	300	0.037	0.024	0.054	0.035
γ-MnO_2-20h	264	275	0.091	0012	0.20	0.026
δ-MnO_2-10h	270	289	0.056	0.036	0.090	0.058
δ-MnO_2-48h	251	258	0.097	0.017	0.52	0.091

a. $R(\mu mol\ min^{-1}) = v_{Tol} \cdot x_{Tol}$, where, $x_{Tol}(\%) = \frac{c_{in} - c_{out}}{c_{in}} \cdot 100\%$

b. $R_s(\mu mol\ m_{cat}{}^{-2} min^{-1}) = \frac{v_{Tol} \cdot x_{Tol}}{W_{cat} \cdot S_{cat}}$

The stability of the catalyst will determine its potential application to some extent. In this study, the cycle stability experiments were performed on the α-MnO_2-10h and δ-MnO_2-48h catalysts, as displayed in Figure 11. It clearly indicated that the catalytic activity of α-MnO_2-10h catalyst decreased with increasing of cycle testing times. The temperature of T_{90} increased to 261 °C after three cycle testing, from 248 °C for the first cycle experiment. On the contrary, the δ-MnO_2-48h catalyst exhibits a good cycle stability, the temperature of T_{90} was maintained at about 255 °C for second and third cycle experiments, which is even lower than that of the fresh catalyst (258 °C), which probably rising from the activated effect occurred after the thermal treatment at 310 °C.

According to literature, the absorbed toluene can be simultaneously oxidized by both adsorbed surface oxygen and lattice oxygen, the adsorbed surface oxygen tends to work at low

temperature (the Langmuir–Hinshelwood), but lattice oxygen always interacts with toluene (Mars–van Krevelen) at high temperature and replenished by adsorbed oxygen via oxygen vacancies or defect sites [28]. Herein, the loss of activity of α-MnO_2-10h catalyst probably derived from the difficulty of replenishing of lattice oxygen. Conversely, it's worth to mention that heterocations K^+ in the mezzanines of layer stack of δ-MnO_2-48h catalyst may play a positive role in improving the emerge-annihilate cycling of oxygen vacancies, to enhance its cycle stability, as reported by Peng et al [22].

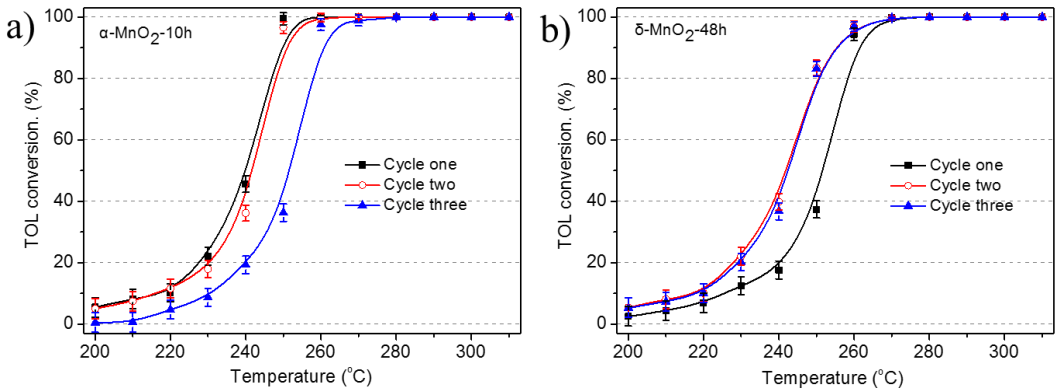

Figure 11 Cycle catalytic stability of MnO_2 catalysts for toluene oxidation (reaction condition: 100 mg catalyst; 1000 ppm toluene; GHSV=30 000 ml/(g·h)).

3.6 Catalytic mechanism discussion

It was reported that the catalytic activity of MnO_2 based catalysts mainly hinges on the physicochemical factor such as specific surface area, concentration of lattice and surface oxygen, K^+ concentration, the adsorptive energy for VOCs, the reduction properties and so on [29, 30]. For the factor of specific surface area, we compared the specific reaction rate of MnO_2 catalyst with different crystalline structure at the reaction temperature of 240 °C, as displayed

in Table 3. We observed that there appeared some relationships between the catalytic activity and specific surface area of MnO_2 catalysts, the specific activity rate of β-MnO_2-10h and δ-MnO_2-10h catalysts were 0.024 and 0.036 μmol/(m^2·min), which are higher than that of γ-MnO_2-20h (0.012 μmol/(m^2·min)). However, the catalytic activity of γ-MnO_2-20h (0.091 umol/min) is superior to that of β-MnO_2-10h (0.037 umol/min) and δ-MnO_2-10h (0.056 umol/min) catalysts. This is evidenced that the improvement of specific surface area can induce the promotion of catalytic activity for the catalysts with a poor intrinsic activity. The enhanced toluene degradation activity of δ-MnO_2-48h can also account for it, but its catalytic activity was inferior to that of α-MnO_2-10h catalyst at low reaction temperature, this phenomenon should be attributed to the difference of intrinsic activity. Moreover, we also observed that the specific activity rate rises along with the increasing of the reaction temperature, the enhanced capacity of catalytic activity for δ-MnO_2-48h was obviously higher than that of other catalysts. It may be assumed to activated effect of surface catalytic sites under the relative high reaction temperature, which can be used to elucidate the reason why the catalytic activity was slightly improved for the spent δ-MnO_2-48h catalyst.

Based on the above analysis, the catalytic activity can be improved by regulating the specific surface area of catalyst to some extent, but it's not the absolute control factor for MnO_2 catalyst with different crystalline structure. As shown in Figure 9 and Table 3, α-MnO_2-10h and δ-MnO_2-48h exhibit a better catalytic capacity than that of γ-MnO_2-20h, owning to their higher surface vacancy oxygen content. From the results of H_2-TPR and XPS, it can be seen that the γ-MnO_2-20h and β-MnO_2-10h catalysts possess the lower lattice oxygen concentration and the lowest reduction capacity or lattice oxygen mobility, which lead to the lowest catalytic activity.

The results are consistent with what reported in the literature that α-MnO_2 NR (nano rod) with a higher availability of lattice oxygen showed a higher CO oxidation activity than that of β-MnO_2 NR [31]. The catalytic activity of δ-MnO_2-10h was slight inferior to that γ-MnO_2-20h, which is mainly attributed to the lower specific surface area or surface oxygen concentration. The α-MnO_2-10h with the lowest reduction temperature and a relative high concentration of lattice oxygen performs the best catalytic capacity for toluene combustion. It was inferred that vacancy oxygen / lattice oxygen concentration, and reduction property are the controlling factors of catalytic activity for MnO_2 catalysts. Furthermore, the catalytic activity was significant enhanced by tuning the hydrothermal conditions for MnO_2 with the same crystalline structure, and the abatement of toluene (cycle stability) on δ-MnO_2 was superior to that on α-MnO_2-10h catalyst, which was attributed to the high lattice oxygen concentration, better lattice oxygen mobility, moderating effect of K^+, and larger specific surface area.

4. Conclusion

Series of MnO_2 catalysts with different crystalline phase (α-, β-, γ- and δ-) have been synthesized under different hydrothermal conditions, and applied in the toluene combustion reaction. Various characterization techniques such as XRD, BET, SEM, TEM, H_2-TPR and XPS were employed to analyze the structure-activity relationship between physicochemical factors such as crystal phase, specific surface area, Mn valence state, lattice oxygen and its mobility and catalytic activity. It was found that the intrinsic activity of MnO_2 varies from the crystal phase, and their catalytic activity mainly depends on their vacancy oxygen / lattice oxygen concentration and their mobility. Moreover, K^+ possess a better moderating effect for

layer stacked structure in δ-MnO_2 than that of tunnel structure in α-MnO_2. δ-MnO_2-48h exhibits a stronger potential application prospect due to its much better structural and cycle stability.

Acknowledgements

We are grateful to the Chinese Scholarship Council (CSC) for providing Luming's Ph.D. scholarship and Institute of Chemical Engineering and Science (ICES, A*star, Singapore) for financial support. The authors kindly thank Luo Wang for experimental help, Zhan Wang for XPS characterization analysis.

Compliance with ethical standards

Conflict of interest The authors declare that they have no conflict of interest.

Reference

[1] Kamal MS, Razzak SA, Hossain MM (2016) Catalytic oxidation of volatile organic compounds (VOCs)-A review. Atmos Environ 140:17-34.

[2] Zhang ZX, Jiang Z, Shangguan WF (2016) Low-temperature catalysis for VOCs removal in technology and application: A state-of-the-art review. Catal Today 264:270-8.

[3] Liotta LF (2010) Catalytic oxidation of volatile organic compounds on supported noble metals. Appl Catal B: Environ 100(3):403-12.

[4] Schick L, Sanchis R, González-Alfaro V, Agouram S, López JM, Torrente-Murciano L, García T, Solsona B (2019) Size-activity relationship of iridium particles supported on silica for the total oxidation of volatile organic compounds (VOCs). Chem Eng J 366:100-11.

[5] Chung WC, Mei DH, Tu X, Chang MB (2018) Removal of VOCs from gas streams via plasma and catalysis. Catal Rev 60:270-331.

[6] Li WB, Wang JX, Gong H (2009) Catalytic combustion of VOCs on non-noble metal catalysts. Catal Today 148 (1-2):81-7.

[7] Brock SL, Duan NG, Tian ZR, Giraldo O, Zhou H, Suib SL (1998) A review of porous manganese oxide Materials. Chem Mater 10:2619-28.

[8] Xu HM, Yan NQ, Qu Z, Liu W, Mei J, Huang WJ, Zhao SJ (2017) Gaseous Heterogeneous Catalytic reactions over Mn-Based oxides for environmental applications: A critical review. Environ Sci Technol 51(16):8879-92.

[9] Lyu Y, Li CT, Du XY, Zhu YC, Zhang YD, Li SH (2020) Catalytic oxidation of toluene over MnO_2 catalysts with different Mn (II) precursors and the study of reaction pathway. Fuel 262: doi.org/10.1016/j.fuel.2019.116610.

[10] Wang F, Dai HX, Deng JG, Bai GM, Ji KM, Liu YX (2012) Manganese oxides with rod-, wire-, tube-, and flower-like morphologies: highly effective catalysts for the removal of toluene. Environ Sci Technol 46(7):4034-41.

[11] Zhang JH, Li YB, Wang L, Zhang CB, He H (2015) Catalytic oxidation of formaldehyde over manganese oxides with different crystal structures. Catal Sci Technol 5 (4):2305-13.

[12] Liang SF, Teng F, Bulgan G, Zong RL, Zhu YF (2008) Effect of phase structure of MnO_2 nanorod catalyst on the activity for CO oxidation. J Phys Chem C 112:5307-15.

[13] Xie YJ, Yu YY, Gong XQ, Guo Y, Guo YL, Wang YQ, Lu GZ (2015) Effect of the crystal plane figure on the catalytic performance of MnO_2 for the total oxidation of propane. CrystEngComm 17(15):3005-14.

[14] Hou JT, Li YZ, Mao MY, Ren L, Zhao XJ (2014) Tremendous effect of the morphology of birnessite-type manganese oxide nanostructures on catalytic activity. ACS Appl Mater Inter 6(17):14981-87.

[15] Yu P, Zhang X, Yao C, Ma YW (2010) Solution-combustion synthesis of ε-MnO_2 for supercapacitors. Mater Lett 64(1):61-4.

[16] Sing KSW, Everett DH, Haul RAW, Moscou L, Pierotti RA, Rouquerol J, Simieniewska T (1985) Reporting physisorption data for gas-solid systems with special reference to the determination of surface area and porosity. Pure Appl Chem 57:603-19.

[17] Wang X, Xie YC (2001) The promotion effects of Ba on manganese oxide for CH_4 deep oxidation. Catal Lett 72(1/2):51-7.

[18] Luo J, Zhu HT, Fan HM, Liang JK, Shi HL, Rao GH, Li JB, Du ZM, Shen ZX (2008) Synthesis of single-crystal tetragonal α-MnO_2 nanotubes. J Phys Chem. C 112:12594–8.

[19] Jia JB, Zhang PY, Chen L (2016) Catalytic decomposition of gaseous ozone over manganese dioxides with different crystal structures. Appl Catal B: Environ 189:210-8.

[20] Selvaraj AR, Rajendiran R, Chinnadurai D, Kumar GR, Kim H, Senthil K, Prabakar K (2018) Stabilization of cryptomelane α-MnO_2 nanowires tunnels widths for enhanced electrochemical energy storage. Electrochim Acta 283:1679-88.

[21] Yin BS, Zhang SW, Jiang H, Qu FY, Wu X (2015) Phase-controlled synthesis of polymorphic MnO_2 structures for electrochemical energy storage. J Mater Chem A 3(10):5722-9.

[22] Yang WH, Su ZA, Xu ZH, Yang WN, Peng Y, Li JH (2020) Comparative study of α-, β-, γ- and δ-MnO_2 on toluene oxidation: Oxygen vacancies and reaction intermediates. Appl Catal B: Environ 260:118150.

[23] Ji J, Lu XL, Chen C, He M, Huang HB (2020) Potassium-modulated δ-MnO_2 as robust catalysts for formaldehyde oxidation at room temperature. Appl Catal B: Environ;260: 118210-21.

[24] Santos VP, Pereira MFR, Órfão JJM, Figueiredo JL (2010) The role of lattice oxygen on the activity of manganese oxides towards the oxidation of volatile organic compounds. Appl Catal B: Environ 99(1):353-63.

[25] Sun H, Liu ZG, Chen S, Quan X (2015) The role of lattice oxygen on the activity and selectivity of the OMS-2 catalyst for the total oxidation of toluene. Chem Eng J 270:58-65.

[26] Li YH, Wang RH, Hao JM (2010) Role of lattice oxygen and lewis acid on ethanol oxidation over OMS-2 Catalyst. J Phys Chem C 114:10544–50.

[27] Li LM, Luo JJ, Liu YF, Jing FL, Su DS, Chu W (2017) Self-propagated flaming synthesis of highly active layered CuO-δ-MnO_2 hybrid composites for catalytic total oxidation of toluene pollutant. ACS Appl Mater Interface 9(26):21798-808.

[28] Qin Y, Wang H, Dong C, Qu ZP (2019) Evolution and enhancement of the oxygen cycle in the catalytic performance of total toluene oxidation over manganese-based catalysts. J Catal 380:21-31.

[29] Shi FJ, Wang F, Dai HX, Dai JX, Deng JG, Liu YX, Bai GM, Ji KM, Au CT (2012) Rod-, flower-, and dumbbell-like MnO_2: Highly active catalysts for the combustion of toluene. Appl Catal A: Gen 433-434:206-13.

[30] Luo J, Zhang QH, Garcia Martinez J, Suib SL(2008) Adsorptive and acidic properties, reversible lattice oxygen evolution, and Catalytic mechanism of cryptomelane-type manganese oxides as oxidation catalysts. J Am Chem Soc130:3198-207.

[31] Jain N, Roy A (2020) Phase & morphology engineered surface reducibility of MnO_2 nanoheterostructures: Implications on catalytic activity towards CO oxidation. Mater Res Bull 121: 110615.